



A realistic 3D finite element model for simulating multiple rotations of modified milling inserts using coupled temperature-displacement analysis

Muhammed Muaz¹ · Sounak Kumar Choudhury¹

Received: 14 August 2019 / Accepted: 9 February 2020 / Published online: 15 February 2020
© Springer-Verlag London Ltd., part of Springer Nature 2020

Abstract

A 3D finite element model was developed to simulate the flat end milling operation by using two cutting inserts having side flank face textures combined with cutting edge micro-serrations. Coupled temperature-displacement analysis was performed by using a general-purpose software, Abaqus/Explicit. A slot at full radial immersion was cut on the workpiece by performing simulations for multiple rotations of the inserts. The novelty of the work is in avoiding the assumption of predefined chip geometry, in combining several important aspects in a single model as well as in making the appropriate advancement of the tool in to the workpiece during multiple rotations. All these phenomena make the model more realistic. The chip geometry was not predefined unlike various works reported in other studies. The model was validated by experimental results. The temperature of the finished surface predicted by the model was compared with the experimentally measured temperature. It was found that the prediction error for the temperature was about 6.1% only. The model was also able to successfully predict the chip morphology similar to that obtained during experiments. The robust novel model proposed in this study can further be utilized easily for performing investigations into the field of cutting tool modification.

Keywords FEM · Serration · Texture · End mill · Chip morphology · Radial immersion · Multiple rotations

1 Introduction

Cutting tool modification through special patterns generation is one of the state-of-the-art techniques used to enhance the machining performance. Textures on tool faces and serrations on cutting edges were found beneficial because of the reduction in area of contact between the tool faces and the workpiece material. 3D finite element modeling based investigations of the effect of the combination of side-flank face textures and serrated edge cutting tool design will open the new insights. The special pattern considered here was the combination of flank-face textures and cutting edge serrations. Flank face textures reduce the ploughing force and flank wear while the cutting edge serrations reduce the cutting forces by reducing the area of contact.

Rake face texturing was widely investigated and found advantageous [1–7]. The textures along with the lubricants impregnated into them improved the machining performance in terms of reduced cutting forces, surface roughness, cutting temperature, coefficient of friction, etc. The textures acted as micropools for lubricants and showed better performance than flooded lubrication [8]. Therefore, this technique was considered as an alternate method for limiting the application of hazardous cutting fluids in the metal cutting industry. Other such techniques included the use of MQL, cryogenic cooling, dry machining at optimum conditions, vegetable oil-based cutting fluids [9, 10], etc. Different types of textures on the flank face were rarely attempted as compared to the rake face textures. However, the flank face has its own significance in cutting operation. The ploughing force and the flank wear, which is set as the tool life criterion in many cases, are mainly associated with this face. Flank wear determines the stability and reliability of machining and dimensional accuracy [11]. The flank wear rate can be retarded by engraving proper textures on the flank face. The works performed on flank face texturing are mostly based

✉ Muhammed Muaz
muaz@iitk.ac.in

¹ Manufacturing Science Lab, Department of Mechanical Engineering, Indian Institute of Technology Kanpur, Kanpur 208016, India

on the texturing of turning tool. A very few researchers [11, 12] considered flank face textures produced on the milling tool.

There are few examples in the literature in which the combination of rake and flank face textures were also investigated. Fatima and Mativenga, [13] examined the effect of the combination of rake and flank face textures on cutting forces, friction coefficient, and flank wear during orthogonal turning of AISI 4140 steel. Better machining performance of textured tools was observed as compared to the regular one. Friction coefficient and compression ratio were reduced by 18% and 17%, respectively, which were responsible for reduction in cutting and feed forces by 10% and 23%, respectively, [13]. Alagan et al. [14] investigated micro-textured cutting tools used for face turning of alloy 718 with high-pressure cooling. Insert having textures in the form of combination of dimples on the rake face and pyramids on the flank face improved the tool life by 30% as compared to the regular one. The textured patterns were generally generated away from the cutting edge. However, if cutting edge is also modified, it is termed as serrations.

Serrations developed over exactly the cutting edges were also showed improvement in the machining performance. Very little work has been reported in the literature on the serrated cutting tools. The serrated pattern generated over the cutting edge of a cutting tool provides positive effects on the mechanics and stability of milling cutter. As compared to the non-serrated cutters, serrated cutters require lower drive torque for an equal amount of material removal and increased productivity by allowing stable machining at a higher depth of cut [15, 16]. Overall, it is clear from the research on textured and serrated tools that it led to sustainable manufacturing. Moreover, the literature survey provided here revealed the fact that the micro-textures and macro-serrations produced on cutting tools were investigated separately. Production of textures on any or both faces of a cutting tool improved the machining performance. Similarly, the application of a tool having a serrated cutting edge was also found beneficial. The serrated edges reduced the cutting forces, while the flank face textures reduced the ploughing forces due to a decrease in the length of contact between tool and workpiece. However, no FEM study is performed yet to investigate the flank face texture and the serrated cutting edge both developed on the same cutting insert in order to combine the benefits of both of the techniques. Numerical simulation of these types of operation, especially by FE method is rarely found in the literature.

Simulation of slot milling operation, which is a combination of up-milling and down-milling processes, by using a modified cutting tool has not been performed yet. Cutting mechanics of slot end-milling operation with full radial immersion is quite complex due to the inclusion of both of the two processes. Therefore, most of the researchers simplified the operation into a 2-D orthogonal cutting process considering only down-

milling or up-milling. However, the behavior of the process is different in each of these types, especially in slot cutting operation. Accurate prediction of output responses during the process is essential which can be achieved by finite elements analysis, a commonly used and more accurate technique as compared to other techniques like empirical model, etc. In FE models developed so far, simulation of a slot milling operation is rarely realized with general-purpose FE packages. It is desired to build up a simulation, including inserts having distinctive patterns to establish material deformation and the chip formation. More recently, the research in the field of FE simulation of metal cutting problems is now being shifted towards 3-D modeling day by day with the advancement in computing technology [17]. However, most of the authors performed simulation for turning process. A very few works have been reported for 3-D simulations of cutting processes other than turning like drilling [18, 19], ball nose end milling [20], down milling [21], helical milling [17, 22], etc. In most of the 3D models developed for milling operation, the cutting tool was assumed as rigid [23–25], while in the present study this assumption was relaxed.

The 3-D simulation is necessary to introduce the third dimension during the cutting process when the corner radius of the cutting insert was also considered [26] along with the flank face texture and the cutting edge serrations. By introducing axial depth of cut along with the feed rate, cutting velocity, and radial depth of cut, the model is expected to reflect the actual physical process more accurately. Moreover, the bottom flank face of the flat-end milling insert rubs the machined surface perpendicular to the tool axis leading to significant friction. It contributes to the axial forces [26] and the stresses developed in the workpiece after machining. This effect is also included in the proposed simulation considering all three dimensions. In the case of milling operation, chips with variable thickness are developed with the advancement of the tool into the workpiece. Therefore, pre-defined geometry of the chip or the sacrificial layers were not assumed in this study before starting the simulation. This approach made the model more realistic.

It is evident that the literature available on FEM modeling of the textured tool is very limited. Some researchers performed FEM analysis for the tools with little modification on cutting edge, e.g., edge honed, etc. [27]. However, they generally assumed the tool as a rigid body. Özel developed a 3D FE model by using DEFORM 3D software to investigate the influence of edge micro-geometry on PcBN turning tool, assumed as a rigid body [27]. Forces, tool wear, and chip geometry predicted by the model were experimentally validated. Olleak and Özel, developed a 3D finite element model by using DEFORM-3D for performing investigations on micro-textured tools for machining of titanium alloy Ti-6Al-4 V. They developed micro-textures on the rake face of a cutting tool insert and performed orthogonal cutting on a cylindrical

workpiece [28]. They did not compare the results obtained through modeling of textured tools with the experimental results. Only results for the modeling of the non-textured tool were validated with the experimental results. However, in the present study, the modeling of modified tool was validated with experiments. Jinxiang et al. [3] analyzed the stress distribution on the rake face textured tool by using a basic finite element model. Cutting forces obtained from the experiments are applied to the model of the textured insert to perform only static analysis [3]. It was concluded that von Mises stress is almost same along the cutting edge. Hence, the mechanical strength of the insert was not sacrificed by the rake face textures. Lie et al. [8] developed a very basic FEM model of the textured insert. When forces obtained from the experimental work were applied to the modeled insert, stresses were generated over it. These stresses were used to conclude that mechanical strength of the insert was not sacrificed by producing textures on its rake face. The combination of tool texture and tool serration, has not been modeled yet through a general-purpose software such that the simulations can be performed for multiple rotations.

In this paper, the development and application of a 3D FEM model are described for slot cutting operation by utilizing milling inserts on which unique pattern was developed. The developed pattern was a combination of flank-face textures and side-cutting edge serrations. A general-purpose FE package, Abaqus/Explicit was utilized for the development of a realistic 3-D finite element model of slot cutting operation with full radial immersion by using the modified flat end milling inserts. As the metal cutting operation is associated with severe plastic deformation along with heat generation, coupled temperature-displacement analysis was performed. The assumption of predefined chip geometry was relaxed. All critical aspects of the process such as full radial immersion, tool nose radius, axial depth of cut, multiple rotations of cutting inserts, initial clearance between tool and workpiece, and most importantly, appropriate advancement of the tool into the workpiece during the cutting simulation were considered. The novelty of the work lies in the modification of the input file too that makes the model applicable for multiple rotations of the cutting tool. ABAQUS/Explicit, by default, considers only exterior elements during interaction between the two mating surfaces, tool and workpiece in the present case. Therefore, after removal of the elements present at the outer most layer of the workpiece, the tool is unable to cut the elements present beneath the outermost layer and hence the forces decrease after each cutting cycle. Therefore, the input file of the present model is modified in order to incorporate the interaction of the tool with the interior elements. The modification makes it possible to remove the interior elements, which also reflects the actual natural phenomenon. The tool is now allowed to penetrate and cut the workpiece correctly and the forces obtained in all the three cycles are comparable

with each other and are not reducing gradually. Moreover, the milling insert used in the present study was not assumed rigid as assumed in several previously published works for simulation of machining processes. Chip morphology and the cutting temperature were predicted by the model and validated by the experimental results with small prediction errors confirming the robustness of the model. Therefore, the same model can be used with confidence to investigate other output parameters. This paper significantly advanced the fundamentals in the field of improvement of cutting tool performance.

2 Materials and methods

2.1 Fully coupled thermo-mechanical finite element model

The proposed finite element model is described in this section. It has been developed to simulate the slot milling operation using inserts having unique patterns developed over them. Essential aspects of the process were also taken into consideration such as full radial immersion, tool nose radius, non-rigid tool, axial depth of cut, multiple rotations of cutting inserts, initial clearance between tool and workpiece, and most importantly, proper interaction of the tool with the workpiece throughout the cutting simulation. The implementation of all these critical aspects allowed the model to reflect the actual physical phenomenon more accurately. The metal cutting problem is associated with significant heat generation. The main cause of heating is severe plastic deformation of material during cutting. Temperature distribution and the stress analysis are dependent on each other for such problems. Therefore, fully coupled thermal-stress analysis was performed in this work by using coupled temperature-displacement elements to obtain thermal and mechanical solutions simultaneously.

2.2 Algorithm for solving coupled thermal-stress problems

In Abaqus/Explicit [29], thermal and mechanical solution responses are obtained by using explicit forward-difference time integration rule with a lumped capacitance matrix and explicit central-difference integration rule with a lumped mass matrix respectively. Thermal and mechanical solutions are obtained simultaneously by an explicit coupling of the explicit central and forward difference integrations as explained in the following section [29].

The explicit forward-difference time integration rule used in Abaqus/Explicit for solving heat transfer equations can be described as follows:

$$\theta_{i+1}^N = \theta_i^N + \Delta t_{i+1} \dot{\theta}_i^N \quad (1)$$

where, θ_i^N is the temperature at node N and the subscript i refers to the increment number in an explicit dynamic step. At the beginning of the increment, the values of the temperature are computed by using the following equation:

$$\dot{\theta}_i^N = (C^{NJ})^{-1} (P_i^J - F_i^J) \quad (2)$$

where, C^{NJ} , P_i^J , F_i^J are the lumped capacitance matrix, the applied nodal source vector, and internal flux vector, respectively.

Similarly, the explicit central difference integration rule used for solving equations of motion is described as follows:

$$\dot{u}_{i+\frac{1}{2}}^N = \dot{u}_{i-\frac{1}{2}}^N + \frac{\Delta t_{i+1} + \Delta t_i}{2} \ddot{u}_i^N \quad (3)$$

$$u_{i+1}^N = u_i^N + \Delta t_{i+1} \dot{u}_{i+\frac{1}{2}}^N \quad (4)$$

where, u^N is either displacement or rotational degree of freedom. At the beginning of the increment, the acceleration of the body is computed by the following equation:

$$\ddot{u}_i^N = (M^{NJ})^{-1} (P_i^J - I_i^J) \quad (5)$$

where, M^{NJ} , P_i^J , and I_i^J are the mass matrix, applied load vector, and inertial force vector, respectively.

2.2.1 Stability [29]

The explicit integration proceeds by using many small time increments with the conditional stability of the central-difference operator (with no damping) depending on the highest frequency of the system as described in the following equation.

$$\Delta t \leq \frac{2}{\omega_{\max}} \quad (6)$$

If damping is also considered, the stable time increment is given by

$$\Delta t \leq \frac{2}{\omega_{\max}} \left(\sqrt{1 + \varepsilon_{\max}^2} - \varepsilon_{\max} \right) \quad (7)$$

where, ε_{\max} is the fraction of critical damping in the highest frequency mode. The stable time increment is reduced by introducing damping to the solution. In Abaqus/Explicit, high-frequency oscillations are reduced by using a small amount of damping in the form of bulk viscosity.

The stable time increment can be approximated by the following equation:

$$\Delta t \approx \frac{L_{\min}}{c_d} \quad (8)$$

where, L_{\min} and c_d are the smallest element dimension in the mesh and the dilatational wave speed, respectively.

2.2.2 Modeling the part geometries and meshing

The modeled workpiece is also shown in Fig. 1. In the workpiece, a circular tool passage zone was introduced to allow the tool to make a full circular cut in the first cutting cycle. Without this provision, the tool had to make several initial cutting cycles before having full engagement with the workpiece to make a full circular cut. This was not a predefined chip geometry. The chip geometry will be set during the simulation according to the tool-work engagement. During the complete simulation step consisting of four cutting cycles, the tool is expected to engage with that particular circular zone only. Therefore, very fine mesh was generated in this region while the rest of the part had coarse mesh. Approximate size of the elements in the circular sacrificial region was 0.15 mm while in the rest of the part it was 1 mm.

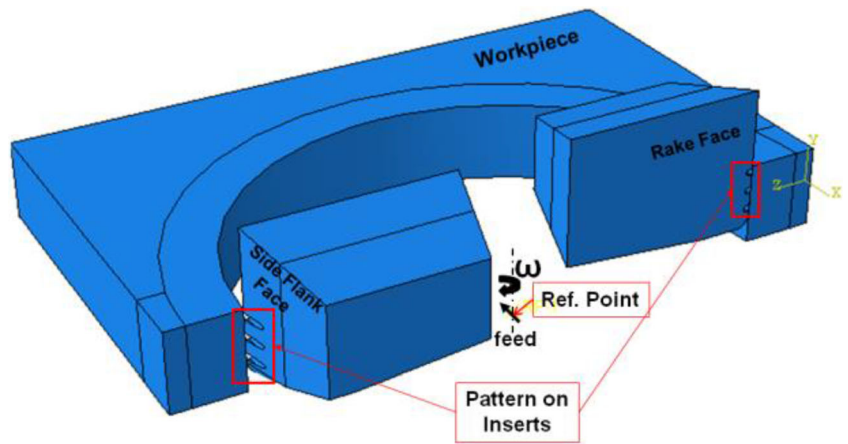
An 8-node thermally coupled hexagonal brick element with reduced integration (C3D8RT) was used, which belongs to the coupled temperature displacement family of explicit element library. Reduced integration was used because it effectively reduces the running time in the 3D analysis by using a lower-order integration to form the element stiffness. However, the mass matrix and distributed loadings use full integration. Hourglass control was managed by an enhanced algorithm; distortion was controlled at length ratio of 0.1, while kinematic split was created at an average strain. Element deletion was enabled to delete the excessively damaged elements from the mesh. These settings were chosen because severe deformation of the elements took place initially followed by element deletion during the cutting simulation. Initial clearance of 0.01 mm was introduced between inserts and the workpiece.

Dimensions of the main features of the insert are shown in Fig. 2. Exactly similar dimensions were used to model the inserts used in simulations. The serrations were made over the side cutting edge of the insert and these were extended toward the side flank face. In other words, the side flank face textures were combined with the serrations. The diameter of the circular cut made on the cutting edge was 200 μm . Center to center distance between the two features was 700 μm . The patterns developed over the inserts are shown in Fig. 3(b). The inserts were meshed with 4-node linear tetrahedral elements (C3D4). Beam-type MPC constraints along with kinematic coupling constraints were assigned to both the inserts. A reference point was defined which mimicked the center of rotation of the cylindrical milling tool. The point was considered as a control point for defining the constraints.

2.2.3 Mesh sensitivity

The size of the mesh elements was selected based on a reduction in the computational cost as well as in the deviation of the simulated results from the experimental ones. Considering both of the two criteria, the size of the elements selected in

Fig. 1 Parts assembly showing modified inserts



the finest mesh region was 0.15 mm. The mesh on the workpiece was generated by sweeping the elements across the circular periphery with the advancing front algorithm. This would lead to appropriate finer mesh with less number of elements. The total number of generated elements on the workpiece was 107,550, with an average aspect ratio of 1.85.

2.2.4 Modeling the tool and work material

The von Mises stresses developed during machining of AISI 4340, a commonly used steel in the aircraft industry for fabrication of structural components [31], has been described in this section. Johnson-Cook constitutive model is best suited for this steel because plastic deformation during milling operation is always associated with large values of strains, strain rates, and thermal effects [29, 32]. The material strength was defined by using the following equation [33].

$$\sigma = (A + B\epsilon^N) \left(1 + C \ln \frac{\dot{\epsilon}}{\epsilon_0} \right) \left[1 + \left(\frac{T - T_r}{T_m - T_r} \right)^m \right] \quad (9)$$

The constitutive constants for Eq.(9) corresponding to AISI 4340 steel are presented in Table 1.

The fracture of the workpiece material takes place when D reaches unity according to the definition given in Eq. (10) as follows:

$$D = \sum \frac{\Delta\epsilon}{\epsilon_f} \quad (10)$$

Where, ϵ_f , defined in Eq. (3), is the equivalent strain to fracture.

$$\epsilon^f = \left[d_1 + d_2 e^{d_3 \frac{\sigma_m}{\sigma}} \right] \left[1 + d_4 \ln \frac{\dot{\epsilon}}{\epsilon_0} \right] \left[1 + d_5 \left(\frac{T - T_r}{T_m - T_r} \right)^m \right] \quad (11)$$

The constant material parameters used in Eq. (9) and Eq. (11) were taken directly from Johnson and Cook’s work [33]. They determined these parameters for AISI 4340 steel. The physical parameters considered for workpiece and tool material are given in Table 2.

Fig. 2 Dimensions of the actual insert [30]

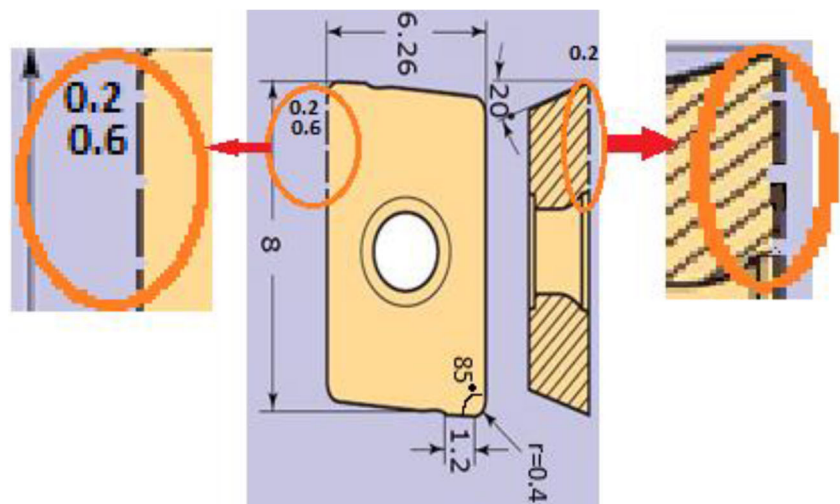
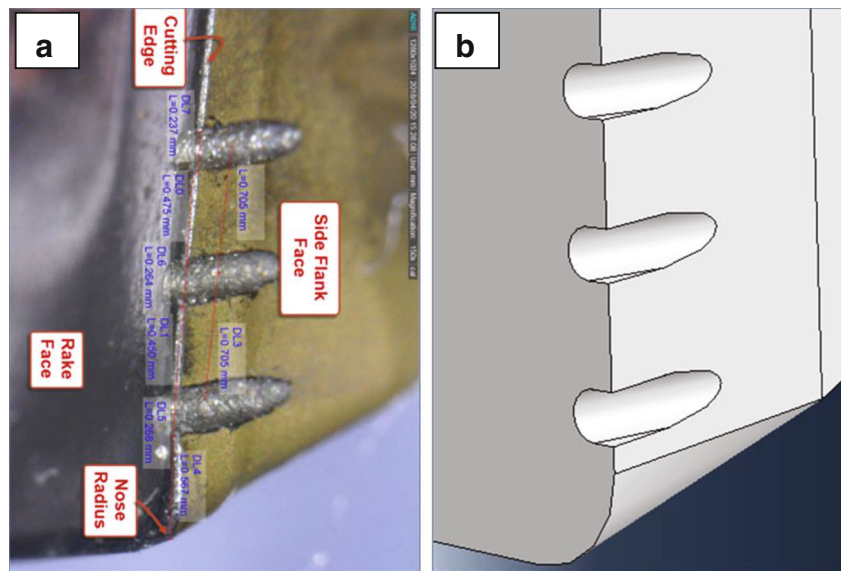


Fig. 3 Patterns developed on the inserts used in experimentation (a) and in simulation model (b)



2.2.5 Modeling the interaction between mating instances

Friction between tool and workpiece was modeled according to a modified Coulomb law [36]. According to this law, different shear stresses were utilized in the sliding as well as in the sticking region, as shown in Fig. 4. The law was defined in Eq. (12) as follows:

$$\tau = \begin{cases} \mu\sigma_n \text{ for } \mu\sigma_n \leq \tau_{max} & ; \text{ Sliding zone} \\ \tau_{max} \text{ for } \mu\sigma_n > \tau_{max} & ; \text{ Sticking zone} \end{cases} \quad (12)$$

If μ and τ_{max} are defined, the Sticking and contact regions will be determined by the model automatically [37].

Tangential behavior of the contact of the instances was defined through penalty contact formulation with a friction coefficient of 0.3, shear stress limit of 456 MPa and with no elastic slip stiffness. Normal behavior was used with hard contact, and separation of the surfaces was allowed after the contact was removed. Contact controls assignment was introduced without any nodal erosion so that the contact nodes of the removed elements are not removed from the contact domain after the erosion of the surrounding faces and edges due to failed elements. If this had not happened, the nodes would flow freely in the contact domain leading to the increase in the computational cost drastically.

General contact type of interaction was allowed to happen in the contact domain, including surface pairs of all with self, including interior surfaces of the domain. This was made possible by the modification in the input file. A new surface defined in the assembly section was assigned to the interior elements of the domain through contact inclusion definition provided in the step section.

Table 1 Input parameters for FEM modeling and cutting conditions

<i>Constitutive constants</i>	
A (MPa)	792
B (MPa)	510
C	0.014
n	0.26
m	1.03
Melting Temperature, T_m (°C)	1520
Room Temperature, T_r (°C)	25
<i>Damage Law Parameters</i>	
Initial failure strain, d1	0.05
Exponential factor, d2	3.44
Triaxiality factor, d3	-2.12
Strain rate factor, d4	0.002
Temperature factor, d5	0.61
<i>Physical Properties</i>	
Density: Workpiece	7850
Tool	11,900
Elastic Modulus: Workpiece	207
Tool	534
Poisson ratio: Workpiece	0.3
Tool	0.2
Friction Coefficient	0.3
Shear stress limit	456
<i>Cutting conditions</i>	
Spindle speed, RPM	7500
Feed Rate, mm/min	1500
Axial depth of cut, mm	2

Table 2 Physical Parameters

Parameters	Workpiece	Tool
Density (Kg/m ³)	7850 [34]	11,900 [30]
Elastic modulus (GPa)	207 [35]	534 [30]
Poisson's ratio	0.3 [35]	0.2 [34]

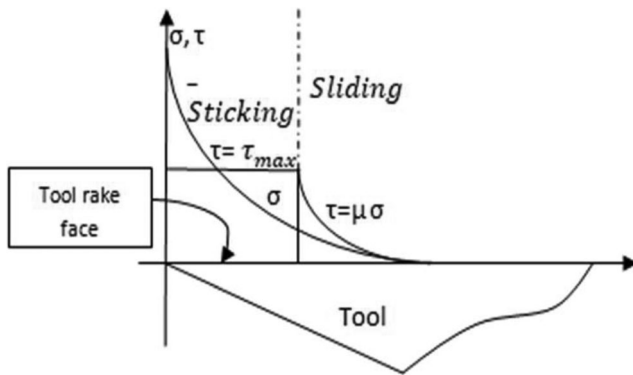


Fig. 4 Stress distribution over tool rake face [38]

2.2.6 Loading and boundary conditions

The linear, as well as rotational velocities, were applied on the reference point defined at the middle of the two inserts. The encastre boundary condition was assigned to the bottom surface of the workpiece so that it remained fixed during the cutting simulations.

2.2.7 Model execution

During 3-D cutting simulation of slot cutting operation, after 180° rotation of an insert, the elements present at the exterior surfaces of the workpiece are removed. Then the elements present in the interior of the workpiece geometry must also start interacting with the second insert properly. Therefore, some modifications in the input file were made and the file was executed in a PC using seven cores of Intel® Core™ i7–2600 CPU at a speed of 3.4 GHz. Eleven licenses of ABAQUS were engaged simultaneously. The simulations were run for approximately 60 h to complete the job for four cutting cycles at the rotational speed of 7500 rpm.

2.2.8 Modification in the input file

ABAQUS/Explicit, by default, considers only exterior elements during the interaction between the two mating surfaces, tool and workpiece in the present case. The contacts between the two instances were made according to the in-built interaction properties, and the contact inclusions were restricted to ‘all exterior’ elements by default. After removal of the elements present at the outer most layer of the workpiece, the elements present in the interior surfaces of the workpiece are exposed to the tool for cutting to progress. However, the tool was unable to cut the workpiece properly, and therefore, the reaction forces were not predicted accurately. Due to the fact that the elements present beneath the outermost layer of the workpiece were not removed properly, forces decreased after each cutting cycle. The average resultant forces for each cutting cycle were plotted in Fig. 5. It can be seen from the figure

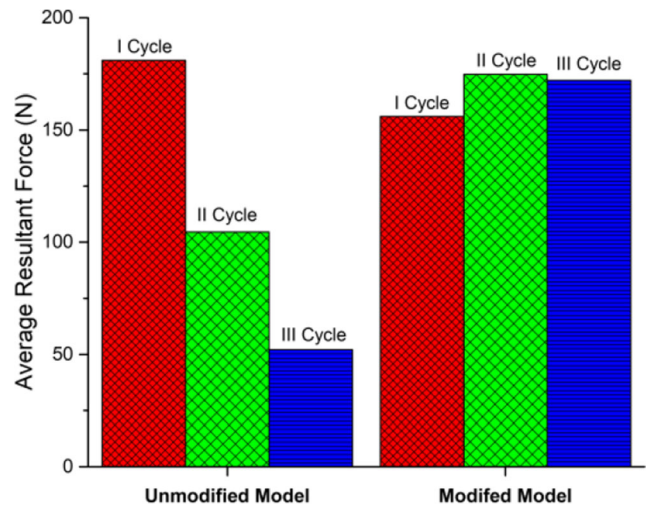


Fig. 5 Comparison of average resultant force obtained by modified and un-modified models

that the force decreased from 181 N to 52 N in three consecutive cycles for the un-modified case. Therefore, the model was modified as described in the next paragraph.

During 3-D cutting simulation, as the tool progressed, the elements present at the exterior surface of the workpiece are removed in the first cycle. Then the elements present in the interior of the workpiece geometry must also start interacting with the cutting tool according to the defined interaction properties. Therefore, in order to incorporate the interaction of the tool with the interior elements, some modifications in the input file were made. First of all, an element set was defined in the assembly that contained all elements that were to be eroded during the cutting process. Interior of the set was called before ending the assembly. Then a surface was defined consisting of elements only. The newly defined surface was then recalled during the simulation with contact inclusions. This surface was assigned to the elements of the workpiece surface exposed to the tool when external surface elements were removed, and the tool penetrated the workpiece beyond the external elements. The nodal erosion was restricted through the contact controls assignment. These modifications made it possible to remove the interior elements, which also reflects the actual natural phenomenon. The tool was allowed to penetrate and cut the workpiece correctly. Now, the forces obtained in all the three cycles were comparable with each other and were not reducing gradually, as shown in Fig. 5 for the modified model.

2.3 Development of the serrated insert

The same features were developed over the insert for performing experiments as in the simulation. The insert was serrated at three points on the main cutting edge by using wire-electric discharge machining such that the serrated points were extended toward the side flank face. In other words, side flank

face textures were combined with the serrated cutting edge. The thickness of the wire of the EDM was 200 μm . The distance between the two cuts was 700 μm . The wire was allowed to enter fully on the rake face so that the depth of the serration was maintained equal to about 200 μm at all three points. A schematic diagram of the insert representing dimensions and the position of serrated cuts is shown in Fig. 2. The rationale for selecting this type of specific texture is to combine the benefits of side-flank face textures and the cutting edge serrations. The textures reduce the ploughing force while the serrations reduce the cutting forces.

2.4 Profiling of the serrated insert

Microscopic images of the developed serrated insert were taken at a magnification of 5X by using Nikon eclipse LV100 Industrial Microscope. The images were taken from the side-flank face as well as from the rake face as shown in Figs. 6 and 7, respectively. Textures were developed over the flank face along with producing serrated cutting edge by generating the grooves at three places. As the whole wire of the wire-EDM having a diameter of 200 μm was allowed to enter at a location during cutting, the diameter of the grooves on the cutting edge was around 201 μm at all three locations. Intensity profile was also shown along with rake face morphology. It was clearly visible from the profile that the cutting edge was modified by generating grooves at three points on the edge.

2.5 Experimentation

Slot cutting operation was performed by using the indigenously modified flat-end milling insert to validate the developed model. A five-axis CNC milling machine (EMCO Concept Mill 250) was used for performing the experiments. The machine tool has the power of 7000 W in the main motor and tool

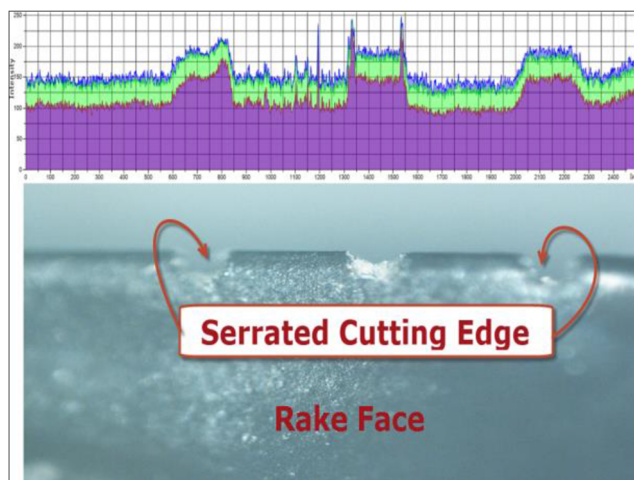


Fig. 6 Profile from rake face side

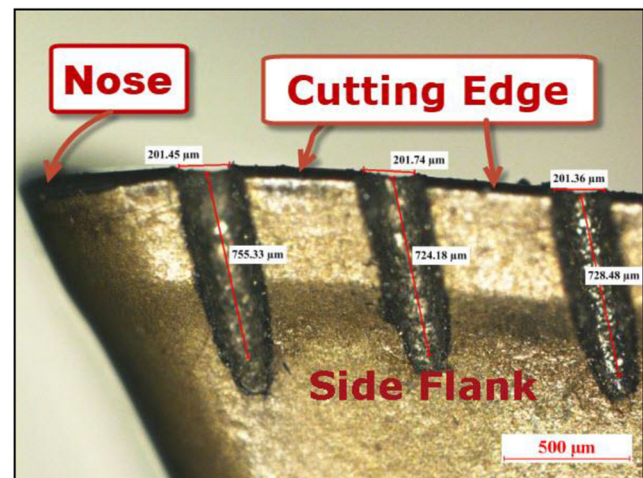


Fig. 7 Profile from flank side

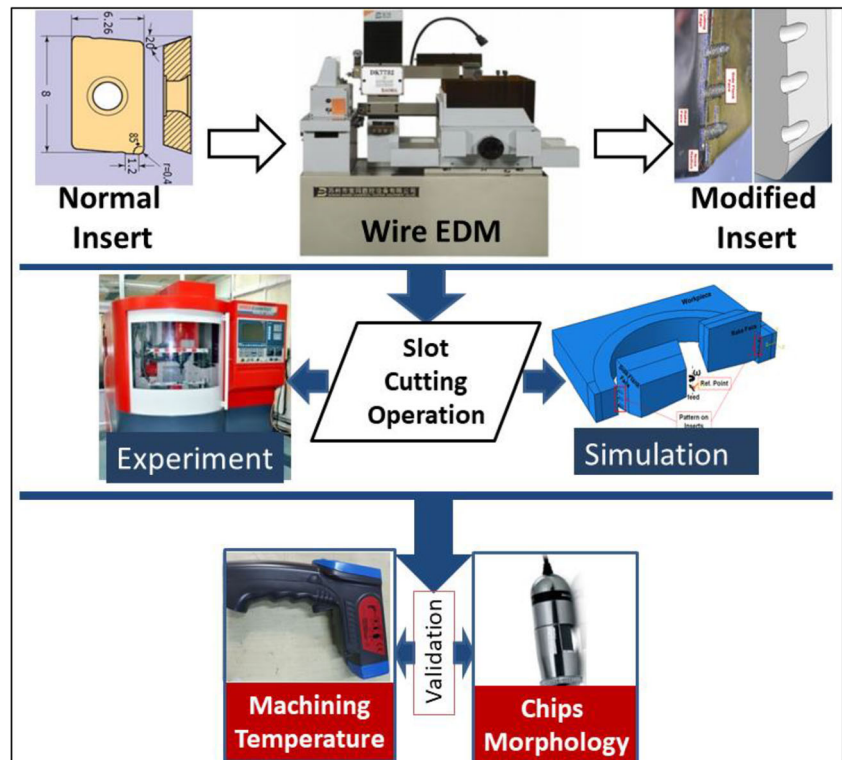
rotation speed of up to 10,000 rpm. The radial depth of cut taken for this study was 16 mm (full radial immersion). Specifications of the tool holder and the insert used in this study were based on the designations F4042.W16.016.Z02.08 and ADMT 080304 R-D56, respectively (Make: Walter tools Ltd.). The material of the work-piece used in this work was AISI 4340 steel. A USB digital microscope (Model: AM7013MZT4 Dino-Lite Premier) with a maximum magnification of 230X and the resolution of 5 Megapixels shown in Fig. 8 was used to observe chips morphology. All the observations were made at a magnification of 50X. The cutting operation was performed at a spindle speed of 7500 rpm and a feed rate of 1500 mm/min. All the machining conditions during experimentation were kept the same as that of the simulation. The whole work plan of simulation and experimental validation is shown in Fig. 8.

3 Results and discussions

3.1 Comparison of temperature

The temperature predicted by the simulated model was probed over the finished surface at different points as shown in Fig. 9. The points labeled in Fig. 9(a) represent the element number followed by the predicted temperature of that element. The average predicted temperature of the machined surface was 40 °C. The temperature was measured online over the finished surface by means of an infrared pyrometer, Eurolab-1250. In order to measure the experimental temperature, the pyrometer was focused over the machined surface just at the end of the slot cut during the milling operation. The temperature of the machined surface was measured at several points in the region shown in Fig. 9(b), and an average was taken. The average temperature of the machined surface was found to be 42.6 °C.

Fig. 8 Work plan



The percentage error between the measured and the predicted temperature was found to be only about 6.1%. The coupled temperature displacement analysis performed in this work is found appropriate for the actual prediction of cutting temperature.

3.2 Comparison of chips morphology

The inserts were successfully able to produce laterally split chips. Split chips were produced during the experimentation as well as through the FEM model. The chips produced from the two methods are compared in Fig. 10. These types of chips are advantageous for machining operations. It predicts the improved machining performance of the modified insert. Partitioning of the chips is

beneficial in metal cutting operations. It shows the reduction in cutting forces as well as the easy removal of chips from the cutting zone. Chip split angle was measured on the chip predicted during the simulation of the cutting operation as shown in Fig. 10(a). The angle was compared by measuring it on the chip produced during experimentation as shown in Fig. 10(b). The prediction error for the angle compared in Fig. 10 was 6.98%. Radii of curvature of the simulated and experimental chips were measured on the locations shown by black curves in Fig. 10(a) and (b), respectively, with the prediction error of 7.14%. Most of the previous models did not predict the chip morphology as similar to the experimental results. Moreover, they were unable to simulate the chips flying away from the machining zone, which actually always happens in real situations.

Fig. 9 Temperature measurement at the machined surface (a) predicted (b) experimental

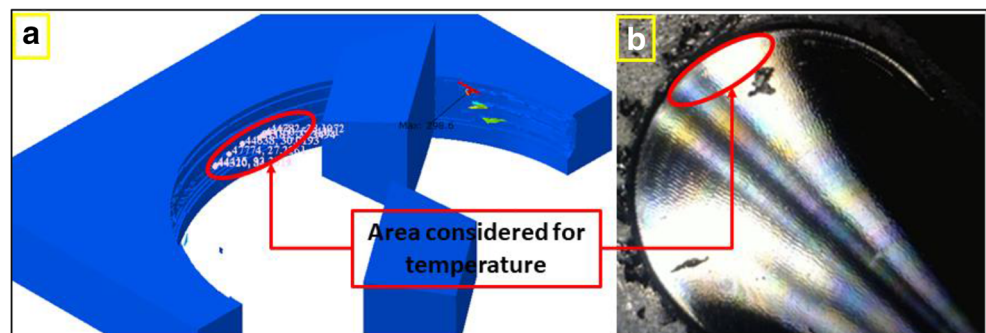
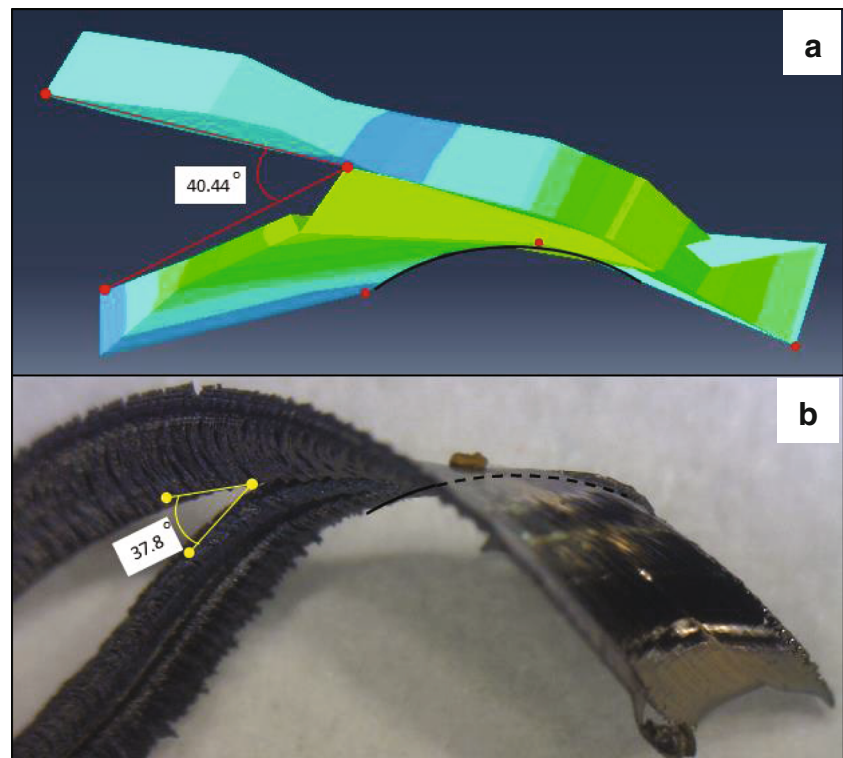


Fig. 10 Chip obtained by (a) simulation and (b) experimentation



3.3 Maximum predicted temperature

The maximum cutting temperature in the machining zone obtained during the machining operation, which is difficult to measure experimentally, can be predicted easily by the model. The maximum temperature predicted by the model was 298.6 °C as shown in Fig. 11. A major part of the heat generated during the machining is due to the plastic deformation of the workpiece material. The chips undergo the maximum deformation as well as the friction with the rake face of the tool. Therefore, the maximum temperature was observed at the chips.

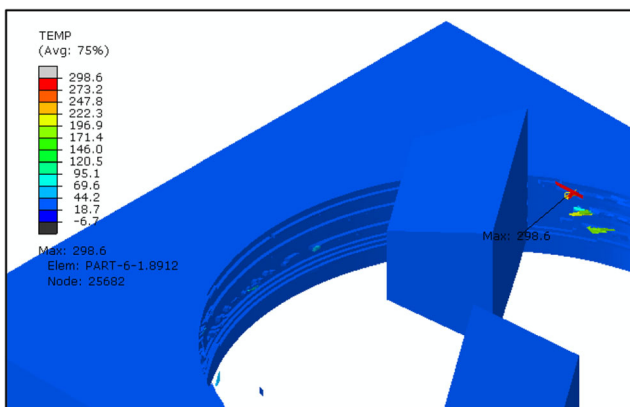


Fig. 11 Maximum predicted temperature

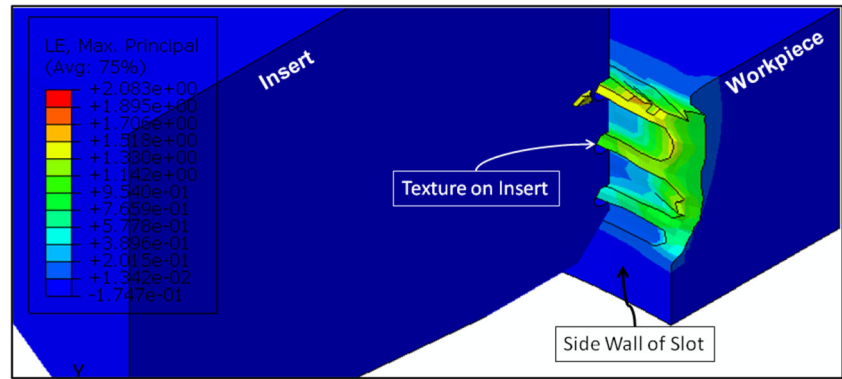
3.4 Predicted morphology of the sidewalls of the slots

The sidewall of the slot cut by the inserts is shown in Fig. 12. The serrations produced over the cutting edge of the insert removed the workpiece material in parts, as shown in Fig. 12 making the material removal process easy and effective. The material protruded from the sidewall was clearly visible, suggesting that the finishing of the sidewall of the slot was sacrificed due to the introduction of the pattern. However, the bottom surface of the slot which is the most important part of the slot remained finished because no serration was provided over the bottom wall of the insert. The sidewall of the slot is comparatively less important. Therefore, the surface roughness of the slot was not supposed to be deteriorated significantly by the serrations produced over the side cutting edge of the inserts. Moreover, the dimension of the pattern is of the order of few microns leading to the surface roughness values of the order of 200 μm only, which is easily tolerable in most of the practical applications.

4 Conclusion

This research added a new significant scientific knowledge in the field of 3D finite element modeling based investigations of the effect of the combination of side-flank face textures and serrated edge cutting tool design. The model was made realistic by avoiding any predefined geometry for the chip and by

Fig. 12 Effectiveness of insert pattern



considering all three dimensions to incorporate nose radius and axial depth of cut along with the radial depth of cut and feed. The novelty lied in the modification of the input file, too, that made the model able to simulate multiple rotations of the cutting tool accurately. The model was experimentally validated with small prediction error of about 6.1%. It was successful in predicting the results by using modified cutting inserts. The surface roughness of the slot was not supposed to be deteriorated significantly by the serrations produced over the side cutting edge of the inserts. The maximum cutting temperature in the machining zone obtained during the machining operation, which is difficult to measure experimentally, was predicted easily. The model can further be utilized for running simulation for further modifications in milling inserts like different textures and serrations. It is a common practice to use textured tools with solid lubricant impregnation, which reduced the coefficient of friction. Therefore, the proper coefficient of friction was also to be introduced along with the developed features.

Acknowledgments Authors are thankful to IIT Kanpur for extending its experimental and computational facilities for performing this research work through 4i Lab, Department of Mechanical Engineering, and the computer center. Moreover, institute fellowship is provided to the corresponding author by the university grants commission of India during this research work.

Compliance with ethical standards

Conflicts of interest (COI) The authors declare that they have no conflict of interest.

References

- Xing Y, Deng J, Zhao J, Zhang G, Zhang K (2014) Cutting performance and wear mechanism of nanoscale and microscale textured $\text{Al}_2\text{O}_3/\text{TiC}$ ceramic tools in dry cutting of hardened steel. *Int J Refract Met Hard Mater* 43:46–58. <https://doi.org/10.1016/j.ijmhm.2013.10.019>
- Gajrani KK, Sankar MR, Dixit US (2018) Tribological performance of MoS_2 -filled microtextured cutting tools during dry sliding test. *J Tribol* 140:021301. <https://doi.org/10.1115/1.4037354>
- Jianxin D, Ze W, Yunsong L, Ting Q, Jie C (2012) Performance of carbide tools with textured rake-face filled with solid lubricants in dry cutting processes. *Int J Refract Met Hard Mater* 30:164–172. <https://doi.org/10.1016/j.ijmhm.2011.08.002>
- Enomoto T, Sugihara T, Yukinaga S, Hirose K, Satake U (2012) Highly wear-resistant cutting tools with textured surfaces in steel cutting. *CIRP Ann - Manuf Technol* 61:571–574. <https://doi.org/10.1016/j.cirp.2012.03.123>
- Obikawa T, Kamio A, Takaoka H, Osada A (2011) Micro-texture at the coated tool face for high performance cutting. *Int J Mach Tools Manuf* 51:966–972. <https://doi.org/10.1016/j.ijmachtools.2011.08.013>
- Sugihara T, Enomoto T (2017) Performance of cutting tools with dimple textured surfaces: a comparative study of different texture patterns. *Precis Eng* 49:52–60. <https://doi.org/10.1016/j.precisioneng.2017.01.009>
- Orra K, Choudhury SK (2018) Tribological aspects of various geometrically shaped micro-textures on cutting insert to improve tool life in hard turning process. *J Manuf Process* 31:502–513. <https://doi.org/10.1016/j.jmapro.2017.12.005>
- Lei S, Devarajan S, Chang Z (2009) A study of micropool lubricated cutting tool in machining of mild steel. *J Mater Process Technol* 209:1612–1620. <https://doi.org/10.1016/j.jmatprotec.2008.04.024>
- Choudhury SK, Muaz M (2020) Natural oils as green lubricants in machining processes. In: Hashmi S, Choudhury IA (eds) *Encycl. Renew. Sustain. Mater.* Elsevier, Oxford, pp 129–136. <https://doi.org/10.1016/B978-0-12-803581-8.10848-3>
- Choudhury SK, Muaz M (2020) Renewable metal working fluids for aluminum and heavy duty machining. In: Hashmi S, Choudhury IA (eds) *Encycl. Renew. Sustain. Mater.* Elsevier, Oxford, pp 242–248. <https://doi.org/10.1016/B978-0-12-803581-8.11546-2>
- Sugihara T, Enomoto T (2013) Crater and flank wear resistance of cutting tools having micro textured surfaces. *Precis Eng* 37:888–896. <https://doi.org/10.1016/j.precisioneng.2013.05.007>
- Muaz M, Choudhury SK (2019) Enhancing the tribological aspects of machining operation by hybrid lubrication-assisted side-flank-face laser-textured milling insert. *J Braz Soc Mech Sci Eng* 41:1–11. <https://doi.org/10.1007/s40430-019-2025-z>
- Fatima A, Mativenga PT (2015) A comparative study on cutting performance of rake-flank face structured cutting tool in orthogonal cutting of AISI/SAE 4140. *Int J Adv Manuf Technol* 78:2097–2106. <https://doi.org/10.1007/s00170-015-6799-6>
- Tamil N, Zeman P, Hoier P, Beno T, Klement U (2019) Investigation of micro-textured cutting tools used for face turning

- of alloy 718 with high-pressure cooling. *J Manuf Process* 37:606–616. <https://doi.org/10.1016/j.jmapro.2018.12.023>
15. Dombovari Z, Altintas Y, Stepan G (2010) The effect of serration on mechanics and stability of milling cutters. *Int J Mach Tools Manuf* 50:511–520. <https://doi.org/10.1016/j.ijmachtools.2010.03.006>
 16. Merdol SD, Altintas Y (2004) Mechanics and dynamics of serrated cylindrical and tapered end Mills. *J Manuf Sci Eng* 126:317–326. <https://doi.org/10.1115/1.1644552>
 17. Ji C, Li Y, Qin X, Zhao Q, Sun D, Jin Y (2015) 3D FEM simulation of helical milling hole process for titanium alloy Ti-6Al-4V. *Int J Adv Manuf Technol* 81:1733–1742. <https://doi.org/10.1007/s00170-015-7323-8>
 18. Guo YB, Dornfeld DA (2000) Finite element modeling of Burr formation process in drilling 304 stainless steel. *J Manuf Sci Eng* 122:612. <https://doi.org/10.1115/1.1285885>
 19. Nan X, Xie L, Zhao W (2016) On the application of 3D finite element modeling for small-diameter hole drilling of AISI 1045 steel. *Int J Adv Manuf Technol* 84:1927–1939. <https://doi.org/10.1007/s00170-015-7782-y>
 20. Soo SL, Dewes RC, Aspinwall DK (2010) 3D FE modelling of high-speed ball nose end milling. *Int J Adv Manuf Technol* 50:871–882. <https://doi.org/10.1007/s00170-010-2581-y>
 21. Wu HB, Zhang SJ (2014) 3D FEM simulation of milling process for titanium alloy Ti6Al4V. *Int J Adv Manuf Technol* 71:1319–1326. <https://doi.org/10.1007/s00170-013-5546-0>
 22. Davoudinejad A, Tosello G, Parenti P, Annoni M (2017) 3D finite element simulation of micro end-milling by considering the effect of tool run-out. *Micromachines*. 8:1–20. <https://doi.org/10.3390/mi8060187>
 23. Marimuthu KP, Prasada HPT, Kumar CSC (2019) Finite element modelling to predict machining induced residual stresses in the end milling of hard to machine Ti6Al4V alloy. *Period Eng Nat Sci* 7:1–7
 24. Thepsonthi T, Özel T (2015) 3-D finite element process simulation of micro-end milling Ti-6Al-4V titanium alloy: experimental validations on chip flow and tool wear. *J Mater Process Technol* 221:128–145. <https://doi.org/10.1016/j.jmatprotec.2015.02.019>
 25. Wang F, Zhao J, Li A, Zhu N, Zhao J (2014) Three-dimensional finite element modeling of high-speed end milling operations of Ti-6Al-4V. *Proc Inst Mech Eng Part B J Eng Manuf* 228:893–902. <https://doi.org/10.1177/0954405413509375>
 26. Adetoro MB, Wen PH (2008) Simulation of End Milling on FEM using ALE Formulation. In: *Conf. Proc. - 2008 Abaqus Users' Conf.* May 19–22, Newport, Rhode Island, USA, pp 1–19
 27. Özel T (2009) Computational modelling of 3D turning : Influence of edge micro-geometry on forces , stresses , friction and tool wear in PcBN tooling. *J Mater Process Technol* 209:5167–5177. <https://doi.org/10.1016/j.jmatprotec.2009.03.002>
 28. Olleak A, Özel T (2017) 3D finite element modeling based investigations of micro-textured tool designs in machining titanium alloy Ti-6Al-4V. *Procedia Manuf* 10:536–545. <https://doi.org/10.1016/j.promfg.2017.07.042>
 29. Abaqus 6.12 Documentation: Analysis User's Manual, Abaqus, Inc. and Dassault Systèmes, 2012
 30. Mabrouki T, Girardin F, Asad M, Rigal JF (2008) Numerical and experimental study of dry cutting for an aeronautic aluminium alloy (A2024-T351). *Int J Mach Tools Manuf* 48:1187–1197. <https://doi.org/10.1016/j.ijmachtools.2008.03.013>
 31. Torres MA, Voorwald HJ (2002) An evaluation of shot peening, residual stress and stress relaxation on the fatigue life of AISI 4340 steel. *Int J Fatigue* 24:877–886. [https://doi.org/10.1016/S0142-1123\(01\)00205-5](https://doi.org/10.1016/S0142-1123(01)00205-5)
 32. Özel T, Zeren E (2007) Finite element modeling the influence of edge roundness on the stress and temperature fields induced by high-speed machining. *Int J Adv Manuf Technol* 35:255–267. <https://doi.org/10.1007/s00170-006-0720-2>
 33. Johnson GR, Cook WH (1985) Fracture characteristics of three metals subjected to various strains , strain rates , temperatures and pressures. *Eng Fract Mech* 21:31–48
 34. Arrazola PJ, Özel T (2010) Investigations on the effects of friction modeling in finite element simulation of machining. *Int J Mech Sci* 52:31–42. <https://doi.org/10.1016/j.ijmecsci.2009.10.001>
 35. Priyadarshini A, Pal SK, Samantaray AK (2012) Influence of the Johnson Cook material model parameters and friction models on simulation of orthogonal cutting process. *J Mach Form Technol* 4:59–83
 36. Guo YB, Liu CR (2002) 3D FEA modeling of hard turning. *J Manuf Sci Eng* 124:189. <https://doi.org/10.1115/1.1430678>
 37. Haglund AJ, Kishawy HA, Rogers RJ (2008) An exploration of friction models for the chip–tool interface using an arbitrary Lagrangian–Eulerian finite element model. *Wear*. 265:452–460. <https://doi.org/10.1016/j.wear.2007.11.025>
 38. Zorev NN (1963) Inter-relationship between shear processes occurring along tool face and shear plane in metal cutting. *Int Res Prod Eng* 49: 143–152

Publisher's note Springer Nature remains neutral with regard to jurisdictional claims in published maps and institutional affiliations.